p–n Heterojunction photoelectrodes composed of Cu₂O-loaded TiO₂ nanotube arrays with enhanced photoelectrochemical and photoelectrocatalytic activities†

Mengye Wang,[a] Lan Sun,*[a] Zhiqun Lin,*[b] Jianhuai Cai,[a] Kunpeng Xie[a] and Changjian Lin*[a]

Cu₂O/TiO₂ p–n heterojunction photoelectrodes were prepared by depositing different amounts of p-type Cu₂O nanoparticles on n-type TiO₂ nanotube arrays (i.e., forming Cu₂O/TiO₂ composite nanotubes) via an ultrasonication-assisted sequential chemical bath deposition. The success of deposition of Cu₂O nanoparticles was corroborated by structural and composition characterizations. The enhanced absorption in the visible light region was observed in Cu₂O/TiO₂ composite nanotubes. The largely improved separation of photogenerated electrons and holes was revealed by photocurrent measurements. Consequently, Cu₂O/TiO₂ heterojunction photoelectrodes exhibited a more effective photoconversion capability than TiO₂ nanotubes alone in photoelectrochemical measurements. Furthermore, Cu₂O/TiO₂ composite photoelectrodes also possessed superior photoelectrocatalytic activity and stability in the degradation of Rhodamine B. Intriguingly, by selecting an appropriate bias potential, a synergistic effect between electricity and visible light irradiation can be achieved.

Broader context

The p-type semiconductor cuprous oxide (Cu₂O) has many advantageous characteristics, such as nontoxicity, low cost, and unique optical and electrical properties, for use in hydrogen production, solar cells, and photocatalysis. Coupling n-type TiO₂ nanotube arrays with Cu₂O nanoparticles enhances the visible light efficiency of TiO₂ nanotubes. The narrow bandgap Cu₂O nanoparticles act as sensitizers to promote the charge transfer to TiO₂, thereby leading to efficient photogenerated charge carrier separation. Such p–n heterojunction photoelectrodes composed of Cu₂O-loaded TiO₂ nanotube arrays exhibit enhanced photoelectrochemical and photoelectrocatalytic activities. As such, it may stand out as a promising candidate for environmental applications in wastewater treatment and the photoinduced splitting of water into hydrogen.

1 Introduction

In recent years, there has been significant interest in controlling environmental pollution and utilizing solar energy. Semiconductor photocatalysis is one of the advanced physicochemical processes applied in the photodegradation of environmental organic pollutants and toxic compounds.[1] Among various oxide semiconductor photocatalysts, TiO₂ has received immense attention due to its outstanding properties, including chemical stability, strong oxidizing activity, corrosion resistance, and nontoxicity.[2–7] Highly ordered TiO₂ nanotube arrays (TiO₂ NTAs)

can be readily fabricated by electrochemical anodization of titanium in fluorine-containing electrolytes[8–13] for use in photoelectrolysis,[14–18] photocatalysis,[19–21] dye-sensitized solar cells,[12,13,22–24] and biological applications.[25–29] However, TiO₂ NTAs used in environmental photocatalysis have two main disadvantages that lead to low utilization efficiency of solar energy. One is the lack of effective absorption in the visible light region due to its wide bandgap ($E_g = 3.2$ eV). The other is that the electron–hole pairs can easily recombine. To this end, a variety of strategies have been developed to improve the visible light absorption, such as doping with metal[30–32] and non-metal[33–35] and coupling with narrow bandgap semiconductors.[36–40] In the latter context, narrow bandgap semiconductors act as sensitizers and facilitate the electron transfer to large bandgap TiO₂ in narrow bandgap semiconductor/TiO₂ heterojunction nanocomposites, thereby efficiently separating photogenerated charge carriers. As a result, the visible light absorption of TiO₂ NTAs and the separation rate of photogenerated electron–hole pairs are substantially increased.

[a]State Key Laboratory of Physical Chemistry of Solid Surfaces, Department of Chemistry, College of Chemistry and Chemical Engineering, Xiamen University, Xiamen, 361005, China. E-mail: sunlan@xmu.edu.cn; cjlin@xmu.edu.cn

[b]School of Materials Science and Engineering, Georgia Institute of Technology, Atlanta, GA 30332, USA. E-mail: zhiqun.lin@mse.gatech.edu

† Electronic supplementary information (ESI) available. See DOI: 10.1039/c3ee24162a

This journal is © The Royal Society of Chemistry 2013

Energy Environ. Sci., 2013, **6**, 1211–1220 | 1211

Cuprous oxide (Cu_2O) represents an important class of metal oxide semiconductor. It has many advantageous characteristics, such as nontoxicity, low cost, and unique optical and electrical properties, for use in hydrogen production, sensors, superconductors, solar cells, and photocatalysis.[41–43] Cu_2O is a relatively narrow bandgap ($E_g = 2.17$ eV) p-type semiconductor,[44] in which both the conduction and the valence bands lie above those of TiO_2.[45] Thus, when TiO_2 is conjugated with Cu_2O, the photogenerated electrons transfer from the conduction band of Cu_2O to that of TiO_2 to form Ti^{3+} center,[45] which extends the lifetime of photogenerated carriers. Moreover, the photoresponse of Cu_2O-conjugated TiO_2 extends into the visible light region.[46]

Herein, we present a *simple yet robust* ultrasonication-assisted sequential chemical bath deposition (S-CBD) technique to yield p-type Cu_2O nanoparticles on n-type TiO_2 NTAs. The photoelectrochemical performance of the resulting Cu_2O/TiO_2 p–n heterojunction composite nanotubes was systematically explored in terms of the amount of Cu_2O loaded on TiO_2 NTAs under both full spectrum and visible light irradiation. Interestingly, by selecting a proper bias potential, a synergistic effect between electricity and visible light irradiation can be reached. Consequently, the photoelectrochemical measurements revealed that Cu_2O/TiO_2 heterojunction photoelectrodes exhibited a more effective photoconversion capability than TiO_2 photoelectrodes alone. Under an appropriate loading of Cu_2O nanoparticles and bias potential, high photoelectrocatalytic activity of Cu_2O/TiO_2 composite photoelectrodes was achieved. The correlated mechanisms of photocatalytic and photoelectrocatalytic degradation of Rhodamine B (RhB) under visible light irradiation were scrutinized. The superior stability of these heterogeneous photocatalysts was examined.

2 Experimental section

2.1 Synthesis of Cu_2O/TiO_2 composite nanotube arrays

The highly ordered TiO_2 NTAs were prepared by electrochemical anodization of Ti foil (0.1 mm thickness, 99.6% purity) in 0.5 wt% HF aqueous solution. Prior to the anodization, Ti foils were ultrasonically cleaned in acetone, alcohol, and distilled water sequentially. The anodization was performed at 20 V for 30 min in a two-electrode cell with Ti foil as the working electrode and platinum foil as the counter electrode at room temperature. After anodization, samples were immediately rinsed with deionized water and dried in air. In order to convert the amorphous phase to the crystalline form, samples were annealed at 500 °C in air for 2 h with a heating rate of 5 °C min^{-1} and a cooling rate of 2 °C min^{-1}. Cu_2O nanoparticles were deposited on the crystalline TiO_2 NTAs by an ultrasonication-assisted sequential chemical bath deposition (S-CBD) method. First, copper acetate ($Cu(CH_3COO)_2 \cdot H_2O$, 0.14 g) was dissolved in absolute ethanol (30 mL). After dark blue solution was formed, polyvinylpyrrolidone (PVP-K30, 0.4 g) was added to the solution and mixed by an ultrasonic generator (KQ2200DB, Kunshan Ultrasonic Instrument Co., Ltd) with a frequency of 99 kHz and an ultrasonic intensity of 2.4 kW m^{-2} for a few minutes. The resulting solution was heated to 40 °C in the water bath. Subsequently, TiO_2 NTAs were immersed into

the solution, followed by the addition of glucose aqueous solution (0.4 g). NaOH (0.14 g) was added to the solution 1 min later. After ultrasonication for different times, the samples were rinsed with distilled water to remove CH_3COO^-, glucose, and NaOH. Finally, the samples were dried under vacuum at a temperature of 60 °C for 2 h.

2.2 Characterization

The morphologies of TiO_2 NTAs and Cu_2O/TiO_2 NTAs were examined by a field-emission scanning electron microscope (FE-SEM, Hitachi S4800) and a transmission electron microscope (TEM, JEM 2100). The crystalline structure of samples was measured by X-ray diffraction (XRD, Philips, Panalytical X'pert, Cu Kα radiation ($\lambda = 1.5417$ Å)). The composition of samples was analyzed by X-ray photoelectron spectroscopy (XPS, VG, Physical Electrons Quantum 2000 Scanning Esca Microprob, Al Kα radiation). The binding energies were normalized to the signal for adventitious carbon at 284.8 eV. UV-visible diffuse reflectance spectra (DRS) of samples were recorded using a UV-vis-NIR spectrophotometer (Varian Cary 5000). Photoluminescence (PL) spectra were obtained using a fluorescence spectrophotometer (Hitachi F-7000) equipped with a xenon lamp as an excitation source ($\lambda_{ex} = 368$ nm).

2.3 Photochemical and photoelectrochemical measurements

Photocurrent density was measured with an Ivium (Compact Stat) using a standard three-electrode configuration composed of the sample as the working electrode, Pt foil as the counter electrode, and saturated calomel electrode (SCE) as the reference electrode in 0.1 M Na_2SO_4. A 300 W Xe lamp with and without a UV-light filter ($\lambda > 420$ nm) was employed as the light source.

2.4 Photocatalytic and photoelectrocatalytic measurements

The visible-light photocatalytic and photoelectrocatalytic activities of Cu_2O/TiO_2 NTAs were evaluated using 5 mg L^{-1} Rhodamine B (RhB) aqueous solution as a model pollutant in a quartz glass reactor. The reactor was equipped with a water jacket to control the reaction temperature. A 500 W tungsten–halogen was utilized as the light source. An optical filter was used to allow visible light (>420 nm) to pass through. At the beginning 10 mL RhB aqueous solution was fed to the reactor. During the measurement, the air was bubbled through the gas disperser into the reactor, and RhB aqueous solution was continuously stirred at 30 °C. After 1 h mixing to establish the adsorption/desorption equilibrium of RhB on the photocatalyst surface, the measurement was initiated by irradiating the light onto the samples. The changes in RhB absorbance were monitored by measuring the maximal absorption at $\lambda = 557$ nm using an UV-vis spectrophotometer (Unico UV–2102 PC, USA). Photoelectrocatalytic measurements were performed in a standard three-electrode configuration with a Cu_2O/TiO_2 NTAs electrode as the working electrode, Pt wire as the counter electrode, and a saturated calomel electrode (SCE) as the reference

1212 | *Energy Environ. Sci.*, 2013, **6**, 1211–1220

This journal is © The Royal Society of Chemistry 2013

electrode, using 0.1 M Na_2SO_4 solution as the electrolyte. All electrodes were connected to a DJS-292C potentiostat.

3 Results and discussion

An ultrasonication-assisted S-CBD method was employed to deposit Cu_2O nanoparticles into vertically aligned TiO_2 nanotubes as well as the interstitial space between nanotubes, yielding the Cu_2O/TiO_2 p–n heterojunction composite nanotubes. The stepwise formation of Cu_2O nanoparticles on TiO_2 NTAs is illustrated as follows. Copper acetate (0.14 g) and polyvinylpyrrolidone (0.4 g) were firstly mixed and formed a blue solution. Subsequently, TiO_2 NTAs were immersed in the solution. Under ultrasonication the air was expelled from the nanotubes, and Cu^{2+} ions diffused and penetrated into the nanotubes. After the addition of glucose and NaOH, Cu^{2+} ions were reduced to Cu^+. Cu_2O nanoparticles were thus formed as depicted in eqn (1).

$$HOCH_2(CHOH)_4CHO + Cu^{2+} + OH^- \rightarrow$$
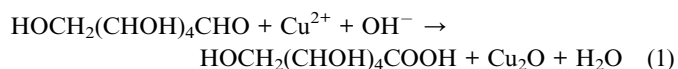$$HOCH_2(CHOH)_4COOH + Cu_2O + H_2O \quad (1)$$

Fig. 1 shows the SEM images of TiO_2 NTAs before (Fig. 1A–B) and after the deposition of Cu_2O at different times using an ultrasonication-assisted S-CBD approach (Fig. 1C–F). The self-organized TiO_2 layer consisted of a dense array of vertically aligned nanotubes with an average tube diameter of 100 nm and a tube length of approximately 400 nm (Fig. 1A and B). After the
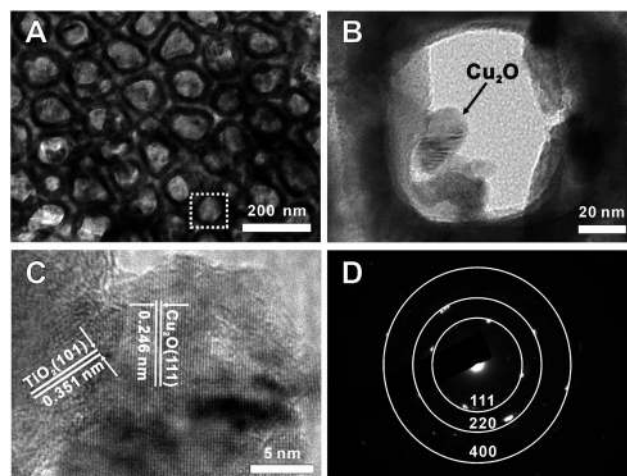
ultrasonication-assisted S-CBD for 4 min, only a few Cu_2O nanoparticles at the entrance of TiO_2 NTAs were observed (Fig. 1C). The corresponding cross-sectional SEM image (Fig. 1D) showed that Cu_2O nanoparticles (marked with arrows) were deposited inside the TiO_2 nanotubes. After the S-CBD for 9 min (Fig. 1E), the amount of Cu_2O nanoparticles deposited on the nanotubes markedly increased. As time progressed to 19 min (Fig. 1F), Cu_2O nanoparticles aggregated to form mulberry-like Cu_2O nanoclusters; some TiO_2 nanotubes were blocked by big nanoclusters. The EDX spectrum reveals that the Cu_2O nanoparticle-loaded TiO_2 NTAs prepared by the S-CBD for 9 min were composed of Cu, Ti, and O elements, where Ti and O peaks resulted from TiO_2 NTAs, and the Cu peak originated from Cu species (Fig. S1, ESI†).

The low magnification TEM image of Cu_2O/TiO_2 NTAs prepared by the ultrasonication-assisted S-CBD for 4 min showed that Cu_2O nanoparticles were successfully formed on the TiO_2 nanotubes (Fig. 2A and B). The average diameter of Cu_2O nanoparticles was 18 nm. Fig. 2C depicts the high resolution TEM image of the selected area, where the lattice fringes of 0.246 nm and 0.351 nm corresponded to the reflections from the (111) plane of Cu_2O and the (101) plane of anatase TiO_2, respectively. The selected area electron diffraction (SAED) pattern taken from the nanoparticles in Fig. 2C revealed that Cu_2O nanoparticles were polycrystalline (Fig. 2D).

The XRD patterns of TiO_2 NTAs and Cu_2O/TiO_2 NTAs are shown in Fig. S2.† The diffraction peaks of TiO_2 NTAs can be indexed to anatase TiO_2 (JCPDS no. 21-1272) and Ti (JCPDS no. 41-1049). For Cu_2O/TiO_2 NTAs, a new diffraction peak at $2\theta = 36.9°$ was observed, which can be ascribed to the (111) plane of cubic Cu_2O (JCPDS no. 05-667). The average size of Cu_2O crystals was 14.2 nm, calculated from the full width at half maximum (FWHM) of the (111) plane using the Scherrer's equation. No Cu and CuO phases were detected in the Cu_2O/TiO_2 NTAs.
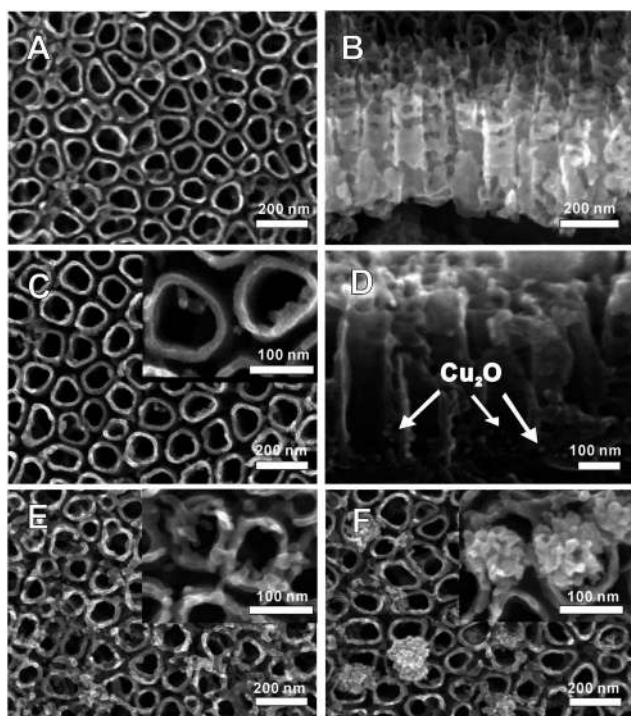
Fig. 1 SEM images of (A and B) TiO_2 NTAs, and (C–F) Cu_2O/TiO_2 NTAs prepared by the ultrasonication-assisted S-CBD of Cu_2O nanoparticles on TiO_2 TNAs for (C and D) 4 min, (E) 9 min, and (F) 19 min. The insets in (C), (E), and (F) are the close-ups of Cu_2O-loaded TiO_2 NTAs. Top view: (A), (C), (E), and (F). Side view: (B) and (D).


Fig. 2 (A) Low magnification TEM image of Cu_2O/TiO_2 NTAs prepared by the ultrasonication-assisted S-CBD for 4 min (top view). (B) Close-up of the selected area marked in (A). (C) The high resolution TEM image of Cu_2O/TiO_2 NTAs. (D) The selected area electron diffraction (SAED) pattern of Cu_2O taken from the nanoparticles in (C).

In order to determine the chemical composition of Cu_2O/TiO_2 composite nanotubes and identify the chemical state of the Cu element in the samples, XPS characterization was performed, from which only Ti, O, C and Cu elements were observed (Fig. 3A). The emergence of the C element can be attributed to adventitious carbon from the sample fabrication and/or the XPS instrument itself. Fig. 3B displays the Cu 2p core level spectrum. The Cu $2p_{3/2}$ and Cu $2p_{1/2}$ spin-orbital photoelectrons were located at binding energies of 932.5 eV and 952.4 eV, respectively, which are in good agreement with the reported values of Cu_2O (i.e., the characteristic peaks of Cu $2p_{3/2}$ for Cu(0), Cu(I), and Cu(II) are at 932 eV, 932.7 eV, and 933.6 eV, respectively[47]). Obviously, the deposited nanoparticles were Cu_2O rather than Cu or CuO. Furthermore, the Cu L_3VV Auger spectrum of Cu_2O/TiO_2 NTAs showed a main peak that appeared at 917.2 eV (Fig. 3C), which was in good agreement with Cu_2O instead of CuO and Cu,[47] further corroborating that the nanoparticles deposited on TiO_2 NTAs were Cu_2O.
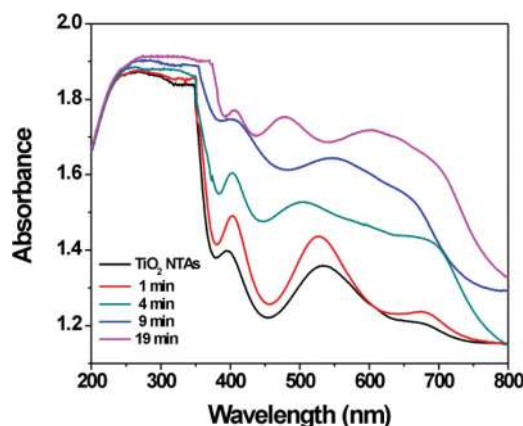
The UV-vis diffuse reflectance spectra (DRS) of pure TiO_2 NTAs and Cu_2O/TiO_2 NTAs prepared at different ultrasonication times are shown in Fig. 4. Clearly, the absorption onset of pure TiO_2 NTAs was at approximately 390 nm, which agreed well with the bandgap of bulk anatase ($E_g = 3.2$ eV, corresponding to $\lambda = 387$ nm). Three additional absorption peaks were observed. The trapped hole exhibited an absorption maximum at $\lambda = 410$ nm, while the trapped electron showed other two absorption maxima at $\lambda = 540$ nm and 690 nm, which can be attributed to the sub-bandgap states of TiO_2 NTAs.[48] Due to the narrow bandgap of Cu_2O ($E_g = 2.17$ eV), all Cu_2O/TiO_2 NTAs displayed red shifts in the bandgap transition and an enhanced absorption in the visible-light region. The optical absorption onsets of Cu_2O/TiO_2 NTAs shifted to the lower energy region with the increased time of ultrasonication-assisted deposition, which may have resulted from the increased amount of Cu_2O nanoparticles formed on TiO_2 NTAs. This suggested that the Cu_2O/TiO_2 composite nanotubes could absorb light over a quite broad spectral range in the visible region, which is a prerequisite for the utilization of visible light for photocatalysis. Therefore, good photochemical and photocatalytic activities of Cu_2O/TiO_2 NTAs under visible light irradiation are expected.
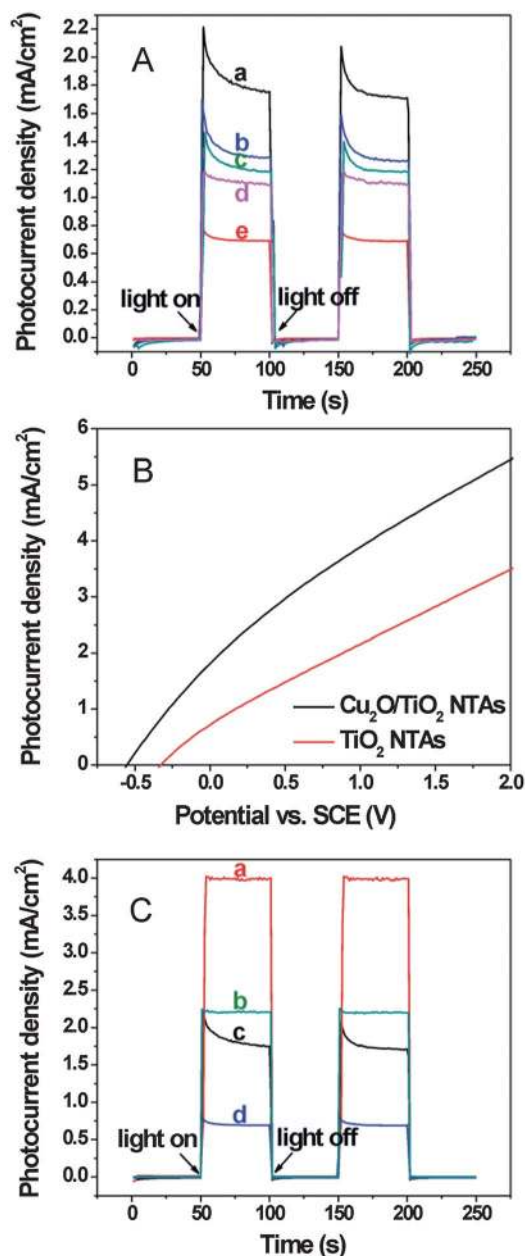
The photochemical and photoelectrochemical behaviors of TiO_2 NTAs before and after the deposition of Cu_2O nanoparticles were explored by measuring the photocurrent response. Fig. 5A presents the photocurrent density–time characteristics of pure TiO_2 NTAs and Cu_2O/TiO_2 NTAs at a 0 V bias vs. saturated calomel electrode (SCE) with a pulse of 50 s under intermittent Xe lamp irradiation (i.e., UV and visible light irradiation). No significant photocurrent density was observed in the dark for all samples. It is clear that the photocurrent densities of all electrodes increased upon illumination. Moreover, the photocurrent densities of all Cu_2O/TiO_2 NTA photoelectrodes were higher than that of pure TiO_2 NTAs. The higher photocurrent density of Cu_2O/TiO_2 NTA photoelectrodes signified an improved optical absorption capability and enhanced separation of photogenerated electrons and holes as compared
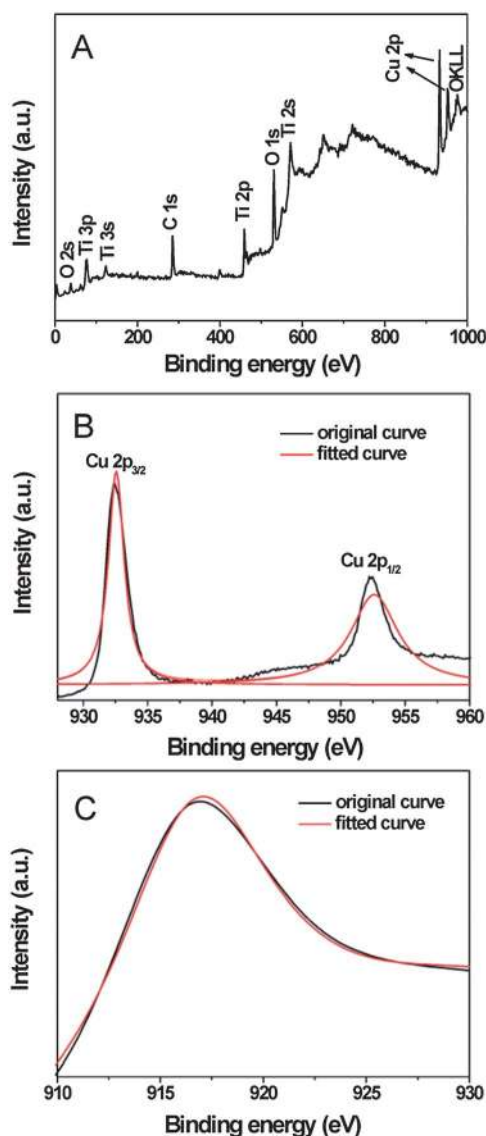
Fig. 3 (A) A XPS survey spectrum of Cu_2O/TiO_2 NTAs. (B) The high resolution XPS spectrum of Cu 2p. (C) The Cu L_3VV Auger spectrum.

Fig. 4 UV-vis diffuse reflectance spectra (DRS) of TiO_2 NTAs and Cu_2O/TiO_2 NTAs prepared by the ultrasonication-assisted S-CBD for different ultrasonication times.

1214 | *Energy Environ. Sci.*, 2013, **6**, 1211–1220

This journal is © The Royal Society of Chemistry 2013

Fig. 5 (A) Photoresponse of Cu_2O/TiO_2 NTAs prepared by ultrasonication-assisted S-CBD for (a) 4 min, (b) 9 min, (c) 1 min, and (d) 19 min and (e) TiO_2 NTAs. (B) Potentiodynamic behaviors (i.e., I–V curves) of Cu_2O/TiO_2 NTAs and TiO_2 NTAs. (C) Photoresponse of Cu_2O/TiO_2 NTAs obtained from the ultrasonication-assisted S-CBD for 4 min (a) with and (c) without a bias potential of 1 V (vs. SCE), and TiO_2 NTAs (b) with and (d) without a bias potential of 1 V (vs. SCE). All the results above were obtained under Xe lamp irradiation (I_0 = 100 mW cm^{-2}).

to TiO_2 NTAs. For the Cu_2O/TiO_2 NTA photoelectrodes, the photocurrent densities increased first and then decreased with an increase of Cu_2O nanoparticle loading, suggesting that the amount of Cu_2O nanoparticles loaded on TiO_2 NTAs can be readily optimized. The highest steady photocurrent density (i.e., 1.83 mA cm^{-2}; curve a in Fig. 5A) was yielded from the 4 min deposition sample, in which only a trace amount of Cu_2O nanoparticles was formed; this was roughly 2.7 times that of pure TiO_2 NTAs (i.e., 0.67 mA cm^{-2}; curve e in Fig. 5A). The

photocurrent was composed of three steps: (i) the photocurrent appeared promptly, (ii) the photocurrent decreased sharply, and (iii) the photocurrent reached a steady state. They are associated with (a) the photogenerated electrons under UV and visible light irradiation, (b) the recombination of photogenerated electron–hole pairs, and (c) the balance of generation and recombination of photogenerated electron–hole pairs, respectively.

The effect of applied potential on the photocurrent response was also investigated by potentiodynamic scans on TiO_2 NTAs and Cu_2O/TiO_2 NTAs. Fig. 5B shows the photocurrent density of the Cu_2O/TiO_2 NTAs photoelectrode obtained from the ultrasonication-assisted S-CBD for 4 min (i.e., the sample possessing the highest photocurrent density; curve a in Fig. 5A) and the pure TiO_2 NTAs photoelectrode under UV and visible light irradiation as the function of applied potential. The photocurrent densities of these two electrodes increased with the increase of bias potential ranging from −0.7 V to 2.0 V vs. SCE. The saturated photocurrent density of Cu_2O/TiO_2 NTAs (i.e., 5.45 mA cm^{-2}) was approximately 1.56 times that of pure TiO_2 NTAs (i.e., 3.49 mA cm^{-2}) at 2.0 V.

Photoelectrochemical behaviors of pure TiO_2 NTAs and Cu_2O/TiO_2 NTAs prepared by ultrasonication-assisted S-CBD for 4 min with and without a 1.0 V bias potential (vs. SCE) are shown in Fig. 5C. Similarly, no photocurrent was observed in the dark. Under UV and visible light irradiation, average photocurrent densities measured on Cu_2O/TiO_2 NTAs with and without a 1.0 V bias potential were 3.98 mA cm^{-2} and 1.78 mA cm^{-2}, respectively; while on TiO_2 NTAs they were 2.21 mA cm^{-2} and 0.69 mA cm^{-2}, respectively. It is not surprising that at the 1.0 V bias potential, average photocurrent densities of the samples apparently increased, which is indicative of much more enhanced charge separation and longer lifetime of photogenerated electron–hole pairs. More importantly, under the 1.0 V bias potential, a steady photocurrent was reached during the entire illumination period for both Cu_2O/TiO_2 NTAs and pure TiO_2 NTAs, suggesting that the bias potential can greatly promote the separation of photogenerated electron–hole of the photocatalyst.

It is noteworthy that the DRS measurements on the Cu_2O/TiO_2 NTAs samples revealed that they exhibited significant visible light response (Fig. 4). Accordingly, the photoelectrochemical behaviors of the TiO_2 NTAs photoelectrode and Cu_2O/TiO_2 NTA photoelectrodes were examined by measuring their photoresponse under the visible light irradiation. The transient photocurrent densities of pure TiO_2 NTAs and Cu_2O/TiO_2 NTAs measured at 0 V bias vs. SCE with a visible light pulse of 50 s are shown in Fig. 6A. The pure TiO_2 NTAs photoelectrode showed no photoresponse under the visible light irradiation due to its wide bandgap. Similarly, as the loading of Cu_2O nanoparticles increased, the photocurrent densities of Cu_2O/TiO_2 NTA photoelectrodes increased first and then decreased, which was in good accordance with the results obtained under UV and visible light irradiation (Fig. 5).

Likewise, the 4 min deposition sample of Cu_2O/TiO_2 NTAs possessed the best photoelectrochemical activity (i.e., curve a in Fig. 6A). The potentiodynamic scans from −0.01 V to 1.00 V vs. SCE were performed on pure TiO_2 NTAs and Cu_2O/TiO_2 NTAs
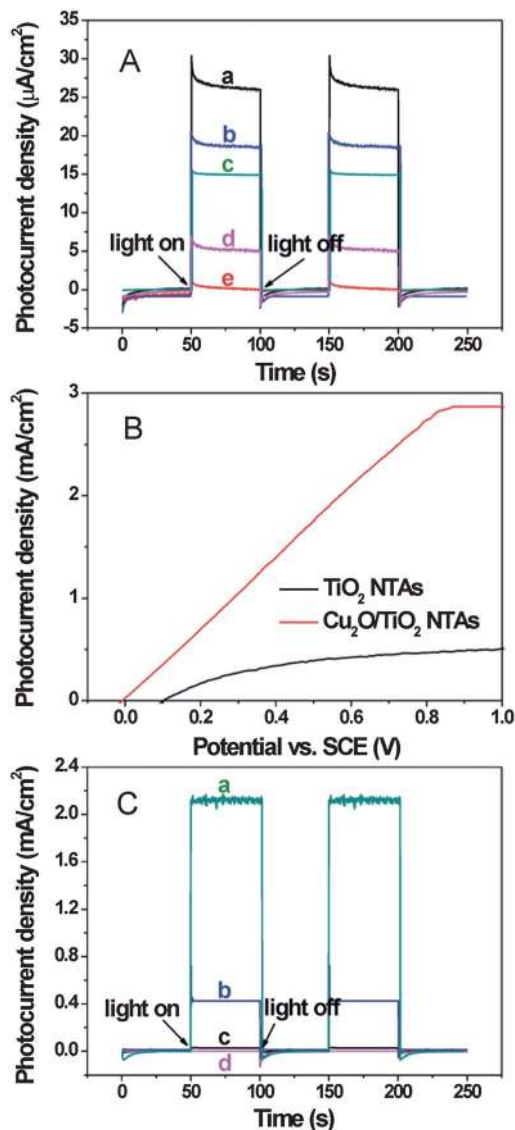
Fig. 6 (A) Photoresponse of Cu_2O/TiO_2 NTAs prepared by ultrasonication-assisted S-CBD for (a) 4 min, (b) 9 min, (c) 1 min, and (d) 19 min and (e) TiO_2 NTAs. (B) Potentiodynamic behaviors (i.e., I–V curves) of Cu_2O/TiO_2 NTAs and TiO_2 NTAs. (C) Photoresponse of Cu_2O/TiO_2 NTAs obtained from the ultrasonication-assisted S-CBD for 4 min (a) with and (c) without a bias potential of 0.5 V (vs. SCE), and TiO_2 NTAs (b) with and (d) without a bias potential of 0.5 V (vs. SCE). All the results above were obtained under *visible light* irradiation ($I_0 = 100$ mW cm^{-2}); this is in contrast to the data in Fig. 5 which was obtained under *Xe lamp* irradiation.

(the 4 min deposition sample) under visible light irradiation (Fig. 6B). The increase in the photocurrent densities was observed with the increase of applied potential, and the increase in the photocurrent density for Cu_2O/TiO_2 NTAs was much more pronounced than that for TiO_2 NTAs. The saturated photocurrent density of the Cu_2O/TiO_2 NTAs photoelectrode (i.e., 2.86 mA cm^{-2}) was about 5.6 times that of the TiO_2 NTAs sample (i.e., 0.51 mA cm^{-2}) in 0.1 M Na_2SO_4. An applied potential of 0.6 V vs. SCE was selected as the proper bias to examine the effect of bias potential on Cu_2O/TiO_2 NTAs and pure TiO_2 NTAs. Similar to the observations in Fig. 5C, under the visible light irradiation the photocurrent densities of the

samples with the bias potential of 0.6 V were much higher than those without the bias potential applied (Fig. 6C). In light of the potentiodynamic behavior noted in Fig. 6B, the photocurrent density of Cu_2O/TiO_2 NTAs (i.e., 2.12 mA cm^{-2}) was 4.98 times that of pure TiO_2 NTAs (i.e., 0.43 mA cm^{-2}) (Fig. 6C), which again implied the increased charge separation rate of photo-generated electron–hole pairs under the bias potential, and the longer lifetime of electron–hole pairs of Cu_2O/TiO_2 NTAs due to the formation of the p–n heterojunction. In addition, Cu_2O/TiO_2 NTAs remained stable after photoelectrochemical measurements (Fig. S4†).

The photocatalytic activities of Cu_2O/TiO_2 p–n heterojunction photoelectrodes on the degradation of Rhodamine B (RhB) under visible light irradiation were also evaluated. Fig. 7A shows the relative concentration variation of RhB solution with different irradiation times for pure TiO_2 NTAs and Cu_2O/TiO_2 NTAs prepared by the ultrasonication-assisted S-CBD for different times. In general, TiO_2 NTAs display the low photo-degradation rate of the organic pollutant under visible light irradiation due to its wide bandgap. However, when RhB was used as the model pollutant, it can be degraded by TiO_2 NTAs as a result of the photosensitization effect of RhB. After 120 min irradiation, 5.40% self-degradation of RhB was seen; while the concentration of RhB was reduced by approximately 10.36%, 25.33%, 31.34%, 19.54%, and 24.96% for TiO_2 NTAs and Cu_2O/TiO_2 NTAs obtained from ultrasonication deposition of Cu_2O nanoparticles for 1, 4, 9, and 19 min, respectively. The linear relationship of $\ln(C/C_0)$ as a function of time (Fig. 7B) suggested
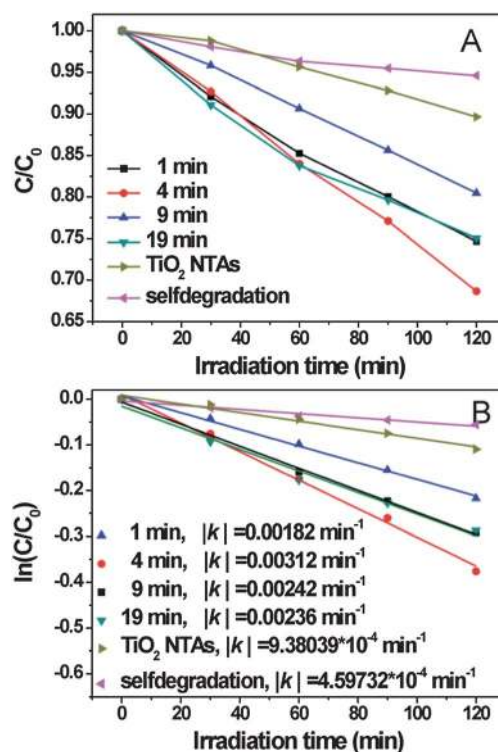
Fig. 7 Photocatalytic degradation rates of RhB under visible light irradiation for TiO_2 NTAs and Cu_2O/TiO_2 NTAs prepared by ultrasonication-assisted S-CBD for different times. (A) C/C_0 vs. t and (B) $\ln(C/C_0)$ vs. t. ($I_0 = 130$ mW cm^{-2}).

1216 | *Energy Environ. Sci.*, 2013, **6**, 1211–1220

This journal is © The Royal Society of Chemistry 2013

Paper   Energy & Environmental Science

that the photocatalytic degradation of RhB followed pseudo-first-order kinetics, which can be expressed by $\ln(C/C_0) = kt$, where $|k|$ is the apparent first-order reaction constant, and C_0 and C are the initial and reaction concentrations of RhB, respectively. The reaction constants, k, for photocatalytic degradation of RhB by pure TiO_2 NTAs and Cu_2O/TiO_2 NTAs prepared by ultrasonication deposition of Cu_2O nanoparticles for 1, 4, 9, and 19 min, were 0.000938, 0.00182, 0.00312, 0.00242, and 0.00236 min^{-1}, respectively. An obvious increase of the RhB degradation rate was found upon the surface modification of TiO_2 NTAs with Cu_2O nanoparticles by ultrasonication for 4 min. However, the RhB degradation rate decreased rapidly when ultrasonication time increased to 9 and 19 min. Clearly, the Cu_2O/TiO_2 NTAs sample obtained from the ultrasonication deposition of Cu_2O nanoparticles for 4 min yielded the optimal photocatalytic performance and had an increase of $|k|$ by about 3.32 times as compared to pure TiO_2 NTAs. The decrease in the photocatalytic activity of the samples prepared after longer ultrasonication time (*i.e.*, 9 and 19 min) suggested that the larger Cu_2O nanoparticles and nanoclusters may act as the electron–hole recombination center, rather than facilitate charge separation,[49] and partially block the channels of TiO_2 nanotubes. The latter was substantiated by SEM measurements (*i.e.*, Fig. 1E and F) and correlated well with the results of photochemical measurements. The blockage of TiO_2 nanochannels reduced the surface area of the photocatalyst, and impeded the wetting of RhB aqueous solution inside the nanotubes. In other words, the deposition of fewer Cu_2O nanoparticles on the TiO_2 nanotubes (*i.e.*, the 4 min deposition) may lead to an effective increase in surface area, thereby promoting photocatalysis (*i.e.*, enhanced photocatalytic activity) together with the enhanced photochemical activity discussed above. The Cu_2O/TiO_2 NTAs and TiO_2 NTAs were further characterized by Photoluminescence (PL) spectra (Fig. S3†). Cu_2O/TiO_2 NTAs showed a much lower PL intensity, indicating that Cu_2O loading resulted in a decrease in the recombination of electron–hole pairs, which could also explain the reason why Cu_2O/TiO_2 NTAs have better photocatalytic activity.

The enhanced photocatalytic activity of TiO_2 NTAs was probably attributed to largely improved visible light absorption and Cu_2O nanoparticle/TiO_2 nanotube heterostructures which favored the charge separation of photogenerated electron–hole pairs after depositing Cu_2O nanoparticles on the TiO_2 NTAs. The charge transfer behaviors during the degradation are schematically illustrated in Fig. 8. The reaction process can be represented in eqn (2)–(13).[45,50,51]
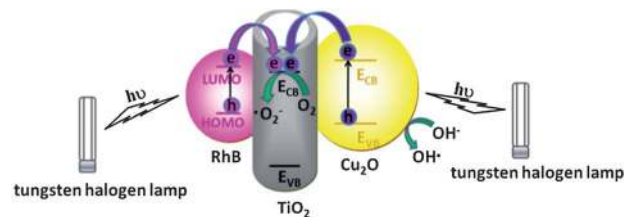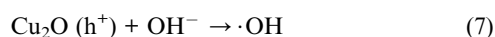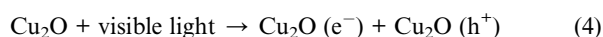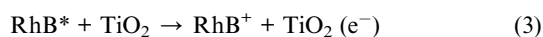
$$RhB + \text{visible light} \rightarrow RhB^* \tag{2}$$

$$RhB^* + TiO_2 \rightarrow RhB^+ + TiO_2\ (e^-) \tag{3}$$

$$Cu_2O + \text{visible light} \rightarrow Cu_2O\ (e^-) + Cu_2O\ (h^+) \tag{4}$$

$$Cu_2O\ (e^-) + TiO_2 \rightarrow TiO_2\ (e^-) \tag{5}$$

$$Cu_2O\ (h^+) + H_2O \rightarrow \cdot OH + H^+ \tag{6}$$

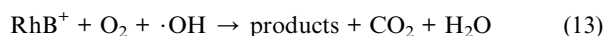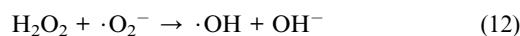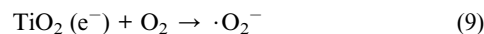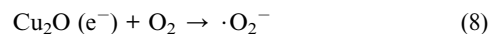$$Cu_2O\ (h^+) + OH^- \rightarrow \cdot OH \tag{7}$$

Fig. 8 Schematic illustration of the mechanism of photocatalytic degradation of RhB using Cu_2O/TiO_2 NTAs as a catalyst under visible light irradiation.

$$Cu_2O\ (e^-) + O_2 \rightarrow \cdot O_2^- \tag{8}$$

$$TiO_2\ (e^-) + O_2 \rightarrow \cdot O_2^- \tag{9}$$

$$\cdot O_2^- + H^+ \rightarrow \cdot OOH \tag{10}$$

$$\cdot OOH \rightarrow H_2O_2 \tag{11}$$

$$H_2O_2 + \cdot O_2^- \rightarrow \cdot OH + OH^- \tag{12}$$

$$RhB^+ + O_2 + \cdot OH \rightarrow \text{products} + CO_2 + H_2O \tag{13}$$

RhB can be excited by visible light due to photosensitization.[50] When TiO_2 NTAs were used as the photocatalyst, RhB molecules were absorbed on the Ti^{4+} sites of TiO_2 NTAs. As the conduction band of TiO_2 is more positive than the oxidation potential of RhB,[51] under the visible light irradiation the excited RhB injected electrons into the conduction band of TiO_2, and RhB molecules became RhB^+ and underwent further reaction to yield final products (eqn (2), (3) and (13)). The electron transfer between RhB and TiO_2 efficiently prevented the recombination of photogenerated electrons and holes and promoted the degradation of RhB. Meanwhile, the p–n heterojunction between n-type TiO_2 nanotubes and p-type Cu_2O nanoparticles was formed after the deposition of Cu_2O nanoparticles on the TiO_2 nanotubes. As Cu_2O with narrow bandgap energy ($E_g = 2.17$ eV) can be easily excited by visible light, and the conduction band of TiO_2 lies more positive than that of Cu_2O, the electrons from the photoexcited Cu_2O can readily transfer to the conduction band of TiO_2 (eqn (4) and (5)), thus favoring prevention of the recombination of photogenerated electrons and holes and facilitating the degradation of RhB. Holes accumulated in the valence band of Cu_2O were consumed by participating in oxidation (eqn (6) and (7)). Accumulated electrons in the conduction band of TiO_2 were transferred to oxygen adsorbed on the surface of TiO_2 to form a superoxide radical anion ($\cdot O^{2-}$), which combined with H^+ to form hydrogen peroxide (H_2O_2) (eqn (8)–(11)). Ultimately, H_2O_2 reacted with $\cdot O^{2-}$ and was reduced to hydroxyl radicals ($\cdot OH$), which further converted RhB^+ to final products (eqn (12) and (13)).

Recently, much attention has been paid to the photoelectrocatalytic approaches to degrade organic pollutants under the UV light irradiation using TiO_2 films as the electrode.[52,53] Under the applied bias potential, the photogenerated electrons move toward the counter electrode, which prevents the recombination of electrons and holes, and thus markedly enhancing

the degradation rate of organic pollutants. Apparently, it is of key importance to choose an appropriate bias potential to increase the degradation rate. To this end, in the present study the most appropriate bias potential for Cu_2O/TiO_2 NTAs was selected to achieve the synergistic effect of the light irradiation and the electricity (*i.e.*, photoelectricity) during the photoelectrocatalytic degradation of organic dye pollutants. As shown in Fig. 6A, the saturated photocurrent density of Cu_2O/TiO_2 NTAs was achieved at 0.8 V. In order to utilize more light energy and less electric energy, the bias potential ranging from 0.2 V to 0.6 V was chosen to degrade RhB. The photocatalysis, electrocatalysis, and photoelectrocatalysis of RhB over Cu_2O/TiO_2 NTAs under visible light irradiation for 15 min were performed. Fig. 9A shows the photocatalysis, electrocatalysis, and photoelectrocatalysis of RhB over Cu_2O/TiO_2 NTAs that were prepared by ultrasonication deposition for 4 min under the visible light irradiation for 15 min. When the bias potential ranging from 0.2 V to 0.4 V was applied, the degradation efficiency of RhB in both electrocatalysis and photocatalysis processes remained unchanged. However, when the bias potential increased from 0.5 V to 0.6 V, the electrocatalytic degradation efficiency became extremely high. Fig. 9B compares the photoelectrocatalytic degradation percentage of RhB with the sum of the photocatalytic and electrocatalytic processes. It is clear that when the bias potential was 0.5 V, the degradation rate of RhB in the photoelectrocatalytic process was much faster than the

expected sum of the electrochemical and photocatalytic processes separately. Accordingly, there was an obvious synergistic effect between the visible light irradiation and the electricity. This synergistic effect can be attributed to the change of the depletion layer of Cu_2O/TiO_2 NTAs. After Cu_2O nanoparticles were deposited on the TiO_2 nanotubes, the depletion layer could form at the heterojunction interface, which hindered the movement of photogenerated electrons and holes by making them pass through it. However, when a positive bias was added on the Cu_2O/TiO_2 NTA photoelectrodes, the depletion layer could become thinner or even disappear, making photogenerated electrons and holes to pass easily. Moreover, the positive bias increased the band bending at the Cu_2O/TiO_2 junction and also facilitated the photo-carrier collection. Therefore, 0.5 V was chosen as the bias potential in the subsequent measurements. Fig. 10 compares the photocatalytic, electrocatalytic, and photoelectrcatalytic degradation of RhB under visible light for Cu_2O/TiO_2 NTAs prepared by ultrasonic-assisted deposition for 4 min. After irradiated under the visible light ($\lambda > 420$ nm) for 20 min, 84.29% of RhB was degraded at a bias potential of 0.5 V, while only 1.45% of RhB was self-degraded and 5.00% of RhB was degraded with the same photocatalyst in the absence of an applied bias potential. In electrocatalytic degradation, 41.07% of RhB was degraded. Obviously, the degradation rate of RhB was improved tremendously by photoelectrocatalysis. The proposed photoelectrocatalytic mechanism is depicted in Fig. 11. When Cu_2O/TiO_2 NTAs immersed in RhB were irradiated with visible light, Cu_2O nanoparticles and RhB were excited, and the photogenerated electrons collected from both Cu_2O and RhB were transferred to the surface of TiO_2 nanotubes. With an applied positive bias potential, the photogenerated electrons travelled vectorially along the long axis of TiO_2 nanotubes and passed the TiO_2/Ti interface to the external circuit, leaving the photogenerated holes in the valence band of Cu_2O and RhB^+. As a result, the degradation rate of RhB was greatly improved.

In addition, the potential reusability and stability of the Cu_2O/TiO_2 NTAs p–n heterojunction photoelectrode in the reaction medium was checked by ten photoelectrocatalytic cycles using Cu_2O/TiO_2 NTAs prepared by ultrasonic-assisted
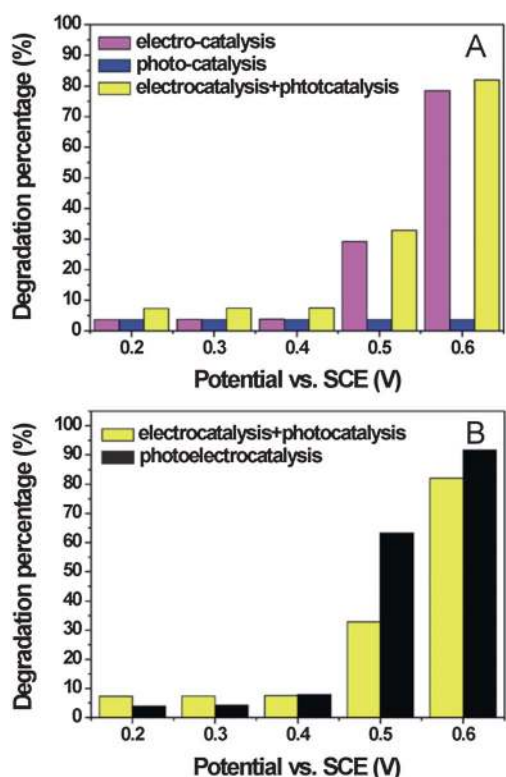
**Fig. 9** (A) RhB degradation efficiencies using Cu_2O/TiO_2 NTAs in photocatalysis (dark blue) and electrocatalysis (purple) after the visible light irradiation for 15 min, and their sum (yellow) at different bias potentials. (B) Comparison of the RhB degradation efficiency using Cu_2O/TiO_2 NTAs in the process of photoelectrocatalysis (black) with the sum from (A) (yellow).
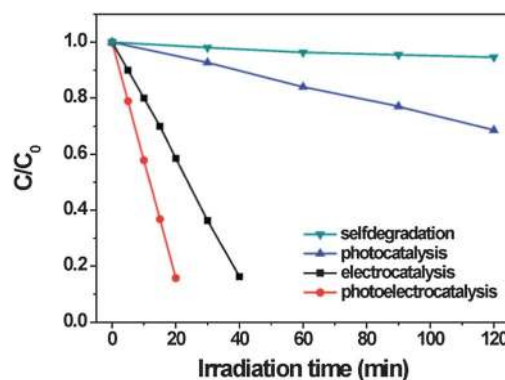
Fig. 10 Comparison of photocatalytic, electrocatalytic, and photoelectrcatalytic degradation of RhB under visible light irradiation for Cu_2O/TiO_2 NTAs prepared by ultrasonication deposition of Cu_2O nanoparticles on TiO_2 NTAs for 4 min.
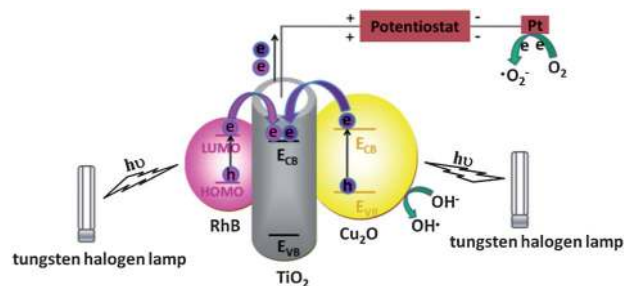
Fig. 11 Schematic illustration of the mechanism of photoelectrocatalytic degradation of RhB using Cu_2O/TiO_2 NTAs as a catalyst under visible light irradiation.

deposition for 4 min that exhibited the highest activity (Fig. 7), which is depicted in Fig. S5.† The removal rate of RhB did not vary significantly after ten cycles. The degradation rate of RhB after the tenth cycle was almost the same as that of the first cycle (Fig. S6†). Fig. S7 and S8,† show the high-resolution XPS spectrum of the Cu window and the SEM image of Cu_2O/TiO_2 NTAs after ten photoelectrocatalytic cycles, respectively. Cu in the Cu_2O/TiO_2 NTAs sample still existed in the form of Cu_2O, and no appreciable change in the surface morphology can be observed. The above results indicated that the Cu_2O/TiO_2 NTA photoelectrodes can remain active for long-term service without much activity degradation, that is, they exhibit excellent photoelectrocatalytic stability.

4 Conclusion

In summary, we crafted Cu_2O/TiO_2 p–n heterojunction photoelectrodes composed of p-type Cu_2O nanoparticles deposited on n-type TiO_2 NTAs by capitalizing on the ultrasonication-assisted sequential chemical bath deposition technique. The visible light response of TiO_2 NTAs was enhanced by the loading of Cu_2O nanoparticles. Notably, the photocatalysts with a small amount of Cu_2O nanoparticles loaded on TiO_2 nanotubes (i.e., obtained from the ultrasonication deposition of Cu_2O nanoparticles for 4 min) exhibited the largest photocurrent and photoconversion efficiency under both UV and visible light irradiation, as well as the highest visible light photocatalytic degradation rate of RhB. In particular, when 0.5 V bias potential was applied, Cu_2O/TiO_2 NTA photoelectrodes were found to possess superior photoelectrocatalytic efficiency due to a synergistic effect of electricity and visible light irradiation, making them promising candidates for environmental applications in wastewater treatment and the photoinduced splitting of water into hydrogen.

Acknowledgements

Notes and references

1 A. Fujishima and K. Honda, *Nature*, 1972, **37**, 238.

2 A. L. Linsebigler, G. Lu and J. T. Yates, *Chem. Rev.*, 1995, **95**, 735.

3 R. Wang, K. Hashimoto, A. Fujishima, M. Chikuni, E. Kojima, A. Kitamura, M. Shimohigoshi and T. Watanabe, *Nature*, 1997, **388**, 431.

4 R. Asahi, T. Morikawa, T. Ohwaki, K. Aoki and Y. Taga, *Science*, 2001, **293**, 269.

5 J. L. Gole, J. D. Stout, C. Burda, Y. B. Lou and X. B. Chen, *J. Phys. Chem. B*, 2004, **108**, 1230.

6 S. Sato, R. Nakamura and S. Abe, *Appl. Catal., A*, 2005, **284**, 131.

7 D. Li, H. Haneda, S. Hishita and N. Ohashi, *Chem. Mater.*, 2005, **17**, 2596.

8 D. Gong, C. A. Grimes, O. K. Varghese, W. C. Hu, R. S. Singh, Z. Chen and E. C. Dickey, *J. Mater. Res.*, 2001, **16**, 3331.

9 J. Wang and Z. Q. Lin, *Chem. Mater.*, 2008, **20**, 1257.

10 J. Wang and Z. Q. Lin, *J. Phys. Chem. C*, 2009, **113**, 4026.

11 J. Wang, L. Zhao, V. S. Y. Lin and Z. Q. Lin, *J. Mater. Chem.*, 2009, **19**, 3682.

12 J. Wang and Z. Q. Lin, *Chem. Mater.*, 2010, **22**, 579.

13 X. K. Xin, J. Wang, W. Han, M. D. Ye and Z. Q. Lin, *Nanoscale*, 2012, **4**, 964.

14 K. Shankar, J. I. Basham, N. K. Allam, O. K. Varghese, G. K. Mor, X. J. Feng, M. Paulose, J. A. Seabold, K. S. Choi and C. A. Grimes, *J. Phys. Chem. C*, 2009, **113**, 6327.

15 N. K. Allam and C. A. Grimes, *J. Phys. Chem. C*, 2009, **113**, 7996.

16 N. K. Allam, K. Shankar and C. A. Grimes, *J. Mater. Chem.*, 2008, **18**, 2341.

17 K. Shankar, G. K. Mor, A. Fitzgerald and C. A. Grimes, *J. Phys. Chem. C*, 2007, **111**, 21.

18 A. C. Grimes, *J. Mater. Chem.*, 2007, **17**, 1451.

19 X. J. Xu, X. S. Fang, T. Y. Zhai, H. B. Zeng, B. D. Liu, X. Y. Hu, Y. Bando and D. Golberg, *Small*, 2011, **7**, 445.

20 J. M. Macak, M. Zlamal, J. Krysa and P. Schmuki, *Small*, 2007, **3**, 300.

21 S. P. Albu, A. Ghicov, J. M. Macak, R. Hahn and P. Schmuki, *Nano Lett.*, 2007, **7**, 1286.

22 P. Roy, S. P. Albu and P. Schmuki, *Electrochem. Commun.*, 2010, **12**, 949.

23 J. G. Chen, C. Y. Chen, C. G. Wu, C. Y. Lin, Y. H. Lai, C. C. Wang, H. W. Chen, R. Vittal and K. C. Ho, *J. Mater. Chem.*, 2010, **20**, 7201.

24 J. R. Jennings, A. Ghicov, L. M. Peter, P. Schmuki and A. B. Walker, *J. Am. Chem. Soc.*, 2008, **130**, 13364.

25 K. Vasilev, Z. Poh, K. Kant, J. Chan, A. Michelmore and D. Losic, *Biomaterials*, 2010, **31**, 532.

26 Y. Y. Song, F. Schmidt-Stein, S. Bauer and P. Schmuki, *J. Am. Chem. Soc.*, 2009, **131**, 4230.

27 L. Peng, M. L. Eltgroth, T. J. LaTempa, C. A. Grimes and T. A. Desai, *Biomaterials*, 2009, **30**, 1268.

28 J. Park, S. Bauer, P. Schmuki and K. von der Mark, *Nano Lett.*, 2009, **9**, 3157.

29 J. Park, S. Bauer, K. von der Mark and P. Schmuki, *Nano Lett.*, 2007, **7**, 1686.

30 I. Paramasivalm, J. M. Macak and P. Schmuki, *Electrochem. Commun.*, 2008, **10**, 71.

31 L. X. Yang, D. M. He, Q. Y. Cai and C. A. Grimes, *J. Phys. Chem. C*, 2007, **111**, 8214.

32 L. Sun, J. Li, C. L. Wang, S. F. Li, Y. K. Lai, H. B. Chen and C. J. Lin, *J. Hazard. Mater.*, 2009, **171**, 1045.

33 X. H. Li, G. Y. Chen, L. B. Yang, Z. Jin and J. H. Liu, *Adv. Funct. Mater.*, 2010, **20**, 2815.

34 J. Lukáč, M. Klementová, P. Bezdička, S. Bakardjieva, J. Šubrt, L. Szatmáry and A. Grusková, *J. Mater. Sci.*, 2007, **42**, 9421.

35 Q. Li and J. K. Shang, *Environ. Sci. Technol.*, 2010, **44**, 3493.

36 S. H. Liu, L. X. Yang, S. H. Xu, S. L. Luo and Q. Y. Cai, *Electrochem. Commun.*, 2009, **11**, 1748.

37 Y. K. Lai, J. Y. Huang, H. F. Zhang, V. P. Subramaniam, Y. X. Tang, D. G. Gong, L. Sundar, L. Sun, Z. Chen and C. J. Lin, *J. Hazard. Mater.*, 2010, **184**, 855.

38 W. T. Sun, Y. Yu, H. Y. Pan, X. F. Gao, Q. Chen and L. M. Peng, *J. Am. Chem. Soc.*, 2008, **130**, 1124.

39 L. X. Yang, B. B. Chen, S. L. Luo, J. X. Li, R. H. Liu and Q. Y. Cai, *Environ. Sci. Technol.*, 2010, **44**, 7884.

40 W. Zhu, X. Liu, H. Q. Liu, D. L. Tong, J. Y. Yang and J. Y. Peng, *J. Am. Chem. Soc.*, 2010, **132**, 12619.

41 S. Deng, V. Tjoa, H. M. Fan, H. R. Tan, D. C. Sayle, M. Olivo, S. Mhaisalkar, J. Wei and C. H. Sow, *J. Am. Chem. Soc.*, 2012, **134**, 4905.

42 J. Y. Zhang, H. L. Zhu, S. K. Zheng, F. Pan and T. M. Wang, *ACS Appl. Mater. Interfaces*, 2009, **1**, 2111.

43 K. Lalitha, G. Sadanandam, V. D. Kumari, M. Subrahmanyam, B. Sreedhar and N. Y. Hebalkar, *J. Phys. Chem. C*, 2010, **114**, 22181.

44 P. E. de Jongh, D. Vanmaekelbergh and J. J. Kelly, *Chem. Commun.*, 1999, 1069.

45 Y. Hou, X. Y. Li, Q. D. Zhao, X. Quan and G. H. Chen, *Appl. Phys. Lett.*, 2009, **95**, 093108.

46 L. Huang, S. Zhang, F. Peng, H. Wang, H. Yu, J. Yang, S. Zhang and H. Zhao, *Scr. Mater.*, 2010, **63**, 159.

47 J. F. Moulder, W. F. Stickle, P. E. Sobol, K. D. Bomben, *Handbook of X-ray Photoelectron Spectroscopy: A Reference Book of Standard Spectra for Identification and Interpretation of XPS Data*, Perkin-Elmer Corporation, 1995.

48 Y. Lai, L. Sun, Y. Chen, H. Zhuang, C. Lin and J. W. Chin, *J. Electrochem. Soc.*, 2006, **153**, 123.

49 Y. J. Zhang, K. F. Li, X. S. Hua, N. H. Ma, D. Chen and H. W. Wang, *Scr. Mater.*, 2009, **21**, 296.

50 P. Qu, J. C. Zhao, T. Shen and H. S. Hidaka, *J. Mol. Catal. A: Chem.*, 1998, **129**, 257.

51 J. Yang, C. C. Chen, H. W. Ji, W. H. Ma and J. C. Zhao, *J. Phys. Chem. B*, 2005, **109**, 21900.

52 Z. Y. Liu, X. T. Zhang, S. Nishimoto, M. Jin, D. A. Tryk, T. Murakami and A. Fujishima, *J. Phys. Chem. C*, 2008, **112**, 253.

53 Z. H. Zhang, Y. Yuan, G. Y. Shi, Y. J. Fang, L. H. Liang, H. C. Ding and L. T. Jin, *Environ. Sci. Technol.*, 2007, **47**, 6259.

1220 | *Energy Environ. Sci.*, 2013, **6**, 1211–1220

This journal is © The Royal Society of Chemistry 2013